Design of Interfacial Electrical Tree-Resistant Packaging Insulation Using Grafted Silicone Elastomer Nanocomposites for High-Temperature Power Modules

Qilong Wang, *Graduate Student Member, IEEE*, Xiangrong Chen, *Senior Member, IEEE*, Ashish Paramane, *Senior Member, IEEE*, Junye Li, Xiaofan Huang, and Na Ren, *Senior Member, IEEE*

***Abstract*—The interfacial electrical tree (IET) between the packaging insulation and the ceramic substrate is easily initiated by a high electric field around the triple point in the power modules, and the IET resistance is not considered in the current packaging insulation design. This article proposes a low-content POSS-grafted silicone elastomer nanocomposite to hinder the IET growth, and its electrical, thermal, and mechanical properties are tested. The IET patterns and the accompanying partial discharge (PD) characteristics are also investigated in the lateral and vertical packaging modules at low and high temperatures. The IET in the packaging modules appears at a much lower voltage than their breakdown voltage and takes longer until the ultimate breakdown of the modules. Besides, the IET is initiated at a lower voltage and grows faster at higher temperatures. The grafted nanocomposite packaging insulation inhibits the IET growth and decreases the IET breakdown probability by its reduced charge carrier mobility and enhanced molecular interaction. The mechanisms of inhibited charge transport on the enhanced electrical properties and hindered IET growth are revealed. Combined with the quantum chemical calculations, bipolar charge transport, and IET phase-field simulations, the design criteria and procedure for high-temperature IET-resistant packaging insulation are proposed.**

Manuscript received 1 September 2023; revised 28 December 2023; accepted 8 February 2024. Date of publication 13 February 2024; date of current version 20 March 2024. This work was supported in part by the Key Project of Natural Science Foundation of Zhejiang Province under Grant LZ22E070001, in part by the National Natural Science Foundation of China under Grant 52007165, in part by the One-hundred Talents Program of Zhejiang University (A), China Scholarship Council under Grant 202306320319, and in part by the Academic Rising Star Program of Zhejiang University under Grant 2022039. Recommended for publication by Associate Editor F. Luo. *(Corresponding author: Xiangrong Chen.)*

Qilong Wang and Xiaofan Huang are with the College of Electrical Engineering, Zhejiang University, Hangzhou 310027, China (e-mail: wangqilong_ql@zju.edu.cn; huangxiaofan123@zju.edu.cn).

Xiangrong Chen is with the College of Electrical Engineering, Zhejiang University, Hangzhou 310027, China, and also with the Zhejiang Provincial Key Laboratory of Power Semiconductor Materials and Devices, Hangzhou Global Scientific and Technological Innovation Center, Zhejiang University, Hangzhou 311200, China (e-mail: chenxiangrongxh@zju.edu.cn).

Ashish Paramane is with the Electrical Engineering Department, National Institute of Technology, Silchar 620015, India (e-mail: ashish@ee.nits.ac.in).

Junye Li and Na Ren are with the ZJU-Hangzhou Global Scientific and Technological Innovation Center, Zhejiang University, Hangzhou 311200, China (e-mail: lijunye@zju.edu.cn; ren_na@zju.edu.cn).

This article has supplementary material provided by the authors and color versions of one or more figures available at https://doi.org/10.1109/TPEL.2024.3365304.

Digital Object Identifier 10.1109/TPEL.2024.3365304

***Index Terms*—Interfacial electrical tree (IET), nanocomposite, packaging insulation, partial discharge (PD), space charge, temperature.**

I. Introduction

HIGH-VOLTAGE SiC power modules are being developed for miniaturization, high temperatures (>175 °C), and voltages (>6.5 kV) for achieving higher power density [1], posing severe challenges to high-temperature packaging insulation design. The interfacial electrical tree (IET) in the power modules is triggered from the triple point due to its high electric field and grows at the interface between the packaging insulation and the ceramic substrate for some time, thereby leading to the ultimate breakdown of the whole modules [2]. However, the current packaging insulation design does not consider IET inhibition but mainly pursues high thermal stability, low hardness, and high dielectric strength [3], [4], [5]. Even if a packaging material has high thermal stability and dielectric strength, IET may be suddenly triggered below the breakdown voltage of the power modules and damage the modules. Besides, the IET research mainly focuses on the low-temperature (<150 °C) silicone gel packaging used in the Si power modules [6], [7]. Notably, the IET and its accompanying PD become more severe with increasing temperature [8], [9]. Therefore, in the high-temperature (>175 °C) packaging insulation design of the SiC power modules, the IET should be considered separately from dielectric strength and thermal stability.

The high electric field near the triple point can be mitigated by modulating packaging structure parameters [10] or coating the nonlinear dielectric materials [11], [12], resulting in a higher partial discharge inception voltage (PDIV) [13]. However, the IET occurrence cannot be eliminated completely due to the inevitable copper protrusions and triple points in the current packaging technology, and the triggered IET still propagates rapidly until the module breaks down. Hence, it is also crucial to hinder IET growth after the IET is initiated.

The nanofillers have been proven to inhibit the electrical tree growth and PD in various polymer materials. The electrical tree growth rate and its PD magnitude are reduced in the nano-SiO_2 doped epoxy resin even at a high temperature of

140 °C [14]. The nano-MgO also inhibits the IET growth and PD magnitude in the cable insulation due to modulated space charge distributions in the nanocomposite [15]. The graphene nanoplatelets reduce the electrical tree length and accumulated area in the silicone elastomer (SE) due to their quantum effect [16]. Moreover, the nanofillers doping can also improve the thermal and insulation properties of the polymers. The nano-BN and nano-SiC doped in SE improve thermal stability, reduce the coefficient of thermal expansion (CTE), and increase the PDIV [17]. The nano-Al_2O_3 is used to improve the high-temperature stability and dielectric strength of SE after high-temperature aging [18], [19]. The nano-SiO_2 doped SE has lower dielectric loss and higher breakdown strength, and the nanocomposite retains a stable insulation property after thermal aging [20]. The nano-AlN-doped epoxy resin is a potential packaging insulation material with high breakdown strength, low electrical conductivity, and low space charge accumulation, which can be used below 150°C [21]. However, there is still a lack of insulation and IET resistance research in the power modules encapsulated by the SE nanocomposites. Moreover, the most common nanofiller doping technique is mechanical stirring and ultrasonic dispersion, and the technique is costly and complicated, easily leading to the aggregation and bad compatibility of fillers in the matrix. In this case, the quantum effects and small-scale effects of nanofillers cannot be fully utilized to maximize the insulation performance.

Compared with the silicone gel operating below several kV and 150 °C [22], the SE exhibits immense potential for high-temperature and high-voltage SiC packaging applications as a soft packaging material due to its high-temperature stability and high dielectric strength above 150 °C [23], [24], [25]. The PD research in the SE encapsulated power module at 110 °C has been reported [26], whereas its selected temperature is still lower than the operation temperature of the SiC power modules above 175 °C, and there is also a lack of IET study at high temperatures. Polyhedral oligomeric silsesquioxane (POSS) is known as the smallest silicon-based compound nanoparticle, only 1–3 nm, and its apex active organic group can be used as a link between the polymer and POSS, thereby enhancing the compatibility between the polymer and POSS, conducive to the chemical grafting and uniform dispersion of the POSS in the polymer [27]. Besides, the bipolar charge transport (BCT) model has been used in the space charge and electric field simulation of the packaging modules [28]. However, the electrical tree phase-field model has only been reported for use in the material simulation so far [29], [30], and it is used for the IET simulation in the power modules for the first time in this article.

In this article, a new SE nanocomposite packaging insulation is proposed to inhibit IET growth. Section II introduces a novel nanofiller-grafting technology that achieves high dispersion and compatibility, even at low filler doping levels, without the drawbacks of traditional techniques. Section III investigates the electrical, thermal, mechanical, and aging properties of the POSS-grafted SE nanocomposite. In Section IV, the IET-resistance performance and accompanying PD characteristics in the lateral and vertical packaging modules are studied at various temperatures, and the effect mechanisms of microscopic charge transport on the electrical properties in the material and the IET growth in the packaging module are analyzed. Section V explores the charge transport and IET growth in the packaging insulation by quantum chemical calculation, BCT simulation, and IET phase-field simulation. Finally, Section VI proposes the IET design criteria and procedure, combining the experimental and simulation results.

II. Material Preparation and Experimental Details

A. Fabrication of POSS-Grafted PMHS and SE Nanocomposite

Vinyl-terminated polydimethylsiloxane (VPDMS, viscosity: 200 mPa·s), polymethyl-hydro siloxane (PMHS, viscosity: 22 mPa·s), Karstedt catalyst (concentration: 3000 ppm), inhibitor and octavinyl-POSS fillers are included in the raw materials. To avoid nanofiller agglomeration and achieve uniform dispersion at an extremely low filler load and high compatibility between the fillers and the polymer, the POSS-grafted PMHS as a new crosslinking agent is fabricated without a costly and inefficient ultrasonic dispersion process (see Fig. S1 and Note S1). The viscosity of the 2 wt% POSS-grafted PMHS is 128 mPa·s with good flowability, higher than the ungrafted PMHS (see Fig. S2). The newly formed chemical bonds in the POSS-grafted PMHS prove that chemical grafting is successful, as shown in the nuclear magnetic resonance spectrum (see Fig. S3 and Note S2). The POSS-grafted PMHS has low contact angles on the surface of Si, Al_2O_3, and Cu (see Fig. S4), exhibiting high affinity with the typical materials in the power modules. The 1 wt%, 2 wt%, and 3 wt% POSS-grafted PMHS are fabricated, respectively.

Here, 12 g VPDMS, 0.25 g POSS-grafted PMHS with different filler loads, 0.05 g Karstedt catalyst, and 0.025 g inhibitor were stirred for 30 min at 25 °C and degassed in a vacuum. Subsequently, the liquid mixture was poured into the flat mold and designed packaging modules to obtain the bulk material and encapsulated module samples, which were then cured at 120 °C for 3 h. The grafted SE nanocomposites made with the 0, 1, 2, and 3 wt% of POSS-grafted PMHS are labeled as SE, SE-POSS 1 wt%, SE-POSS 2 wt% and SE-POSS 3 wt%. The filler load is extremely low in the SE nanocomposite, e.g., the filler content in SE-POSS 2 wt% is only 0.04 wt%. Besides, the fillers disperse well in the polymer without agglomeration (see Fig. S5), as proved by the scanning electron microscope. The SE nanocomposites exhibit excellent adhesion to the surfaces of the copper trace and the ceramic substrate in the encapsulated modules, characterized by the scanning acoustic microscope. Remarkably, no delamination, bubbles, voids, or impurities are detected at their interfaces within the modules (see Fig. S6).

The two packaging modules are designed to be the lateral and vertical types for investigating the IET and its accompanying PD under lateral and vertical electric stress, respectively, as shown in Fig. 1. The geometrical parameters of the two modules are shown in Fig. S7. The high voltage and ground connections are situated on the same side of the lateral module. In particular, the sharp angle of the high-voltage copper trace creates a concentration of high electric field (see Fig. S8), thus facilitating the generation of

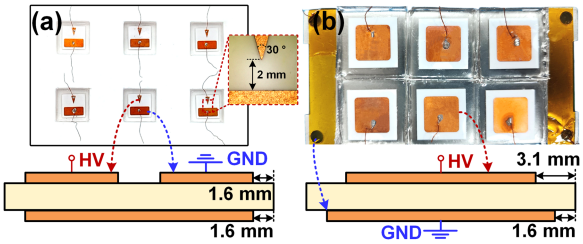

Fig. 1. Electrode shapes and connection methods of the (a) lateral and (b) vertical module.

PD and IET. The high voltage and ground are respectively connected to the two sides of the vertical module. The lower copper, which is longer than the upper copper by an offset of 1.5 mm, rests upon a larger baseplate. As a result of this configuration, the upper copper edge exhibits a significantly elevated electric field (see Fig. S9), thereby facilitating the occurrence of PD and IET on the upper side. Although the vertical module maintains a relatively uniform distribution of electric field around the copper trace in the case of no edge protrusions (see Fig. S10), the inevitable metal protrusions are distributed randomly along the copper edge, causing a high electric field, and initiating the PD and IET.

B. Experimental Details

The thickness of the bulk material samples used for various electrical, thermal, and mechanical characterizations is approximately 0.2 mm. The electrical properties of the SE and its nanocomposites are characterized by electrical conductivity and breakdown strength at 30, 160, and 200 °C. The dc electrical conductivities were assessed by a three-electrode setup (see Fig. S11) at varying dc electric fields of +5, +10, +15, and +20 kV/mm, aiming to study the field-dependence of electrical conductivity. The electrical conductivity and its field-dependent nonlinear coefficient are calculated based on Note S3. The ac breakdown strengths of the materials were measured by the encapsulated sphere-sphere electrodes to avoid surface flashover with the voltage rising rate of 1 kV/s (see Fig. S12). The characteristic breakdown strengths corresponding to a 63.2% probability of sample breakdown are analyzed by a two-parameter Weibull statistic (Note S4).

The microscopic charge transport properties of the SE and its nanocomposites were characterized by surface potential decay (SPD), thermally stimulated depolarization current (TSDC), and space charge. In the SPD experiment, the material surface was charged using a high-voltage electrode related to the process of charge trapping. After the high voltage was removed, the surface potential gradually decayed, indicating the charge detrapping process. The carrier mobility and the time for charges escaping from the traps can be assessed by the SPD differential curve (see Fig. S13 and Note S5). The TSDC curve showcases the release of trapped charges when the temperature rises, used for calculating the density-depth distribution of the charge traps (see Fig. S14 and Note S6). Furthermore, the spatial and temporal distribution of space charge, signifying the position and accumulation of space charge within the material, can be accurately measured by the pulse-electro-acoustic space charge measurement system (see Fig. S15 and Note S7).

The mechanical properties of the SE and its nanocomposites were evaluated through the crosslinking degree, dielectric spectrum, tensile experiment, dynamic mechanical analysis (DMA), and hardness. The crosslinking degree indicates the compactness and density of the molecular structure (Note S8). The dielectric spectrum analyzes the relaxation movements of molecular chains at high temperatures (Note S9). The tensile experiment provides valuable information regarding properties such as tensile strength, elongation at break, and Young's modulus (Note S10). The CTE can be derived from the DMA curve (Note S11). The hardness reflects the material's resistance to external forces, measured by the Shore rubber durometer (Note S12). In terms of thermal properties, thermogravimetric analysis (TGA) under nitrogen was employed to assess weight loss from 20 °C to 800 °C, examining the material's thermal stability, with the derivative thermogravimetry (DTG) indicating the rate of weight loss (Note S13). The thermal conductivity reflects heat dissipation ability, measured by the heat flux method (Note S14).

The ac PD behaviors of the IET in the packaging modules under 30 °C, 160 °C, and 200 °C were measured by the MPD 600 system based on IEC 60270. The background noise of the MPD 600 system is less than 10 pC. The PDIVs were measured ten times for the same condition to maintain accuracy. The PD experimental setup and the test voltage protocol are depicted in Fig. S16 and Fig. S17, respectively. The voltage ascended from 5 kV at a rate of 0.1 kV/s. To hinder interference from transient high-frequency voltage, the ascending interval was set to 2 s, and no PD event was initiated during each rise time. The voltage endured steadily for 5 min during each stage. If a PD failed to occur in the corresponding stage, the voltage would rise to the next stage until a PD is triggered, at this point, the trigger voltage was the PDIV. The IET was triggered by a voltage 1 kV higher than the PDIV to ensure an instant IET initiation, observed by a microscope, and then the phase-resolved partial discharge (PRPD) patterns and IET lengths in the IET growth process were recorded for 5 min after the IET is initiated.

III. Material Testing

A. Effect of Thermal Ageing

The bulk material samples of SE and SE nanocomposites are thermally aged for 500 h under 200 °C in the oxygen-containing environment. The aging properties at 30 °C are shown in Fig. 2. The Weibull curve of breakdown strengths is shown in Fig. S18. The SE nanocomposites have lower weight loss, higher crosslinking degree, lower electrical conductivity, higher field-dependence of conductivity (see Fig. S19), and higher breakdown strength than SE both before and after aging. The crosslinking degree, electrical resistivity, and breakdown strength of the SE nanocomposites become higher after aging, whereas those properties of SE become worse after aging. Besides, no surface crack or interface delamination is observed in the encapsulated modules with the SE nanocomposites after aging (see Fig. S6).

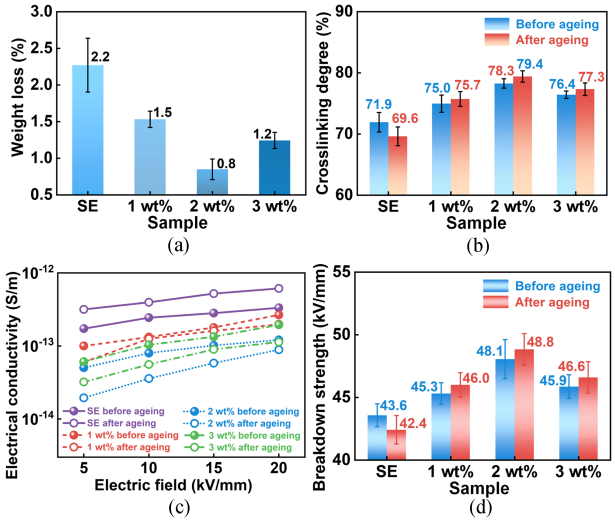

Fig. 2. (a) Weight loss after thermal aging, (b) crosslinking degree, (c) electrical conductivity, and (d) breakdown strength of SE and its nanocomposites before and after thermal aging at 200 °C for 500 h (measured at 30 °C).

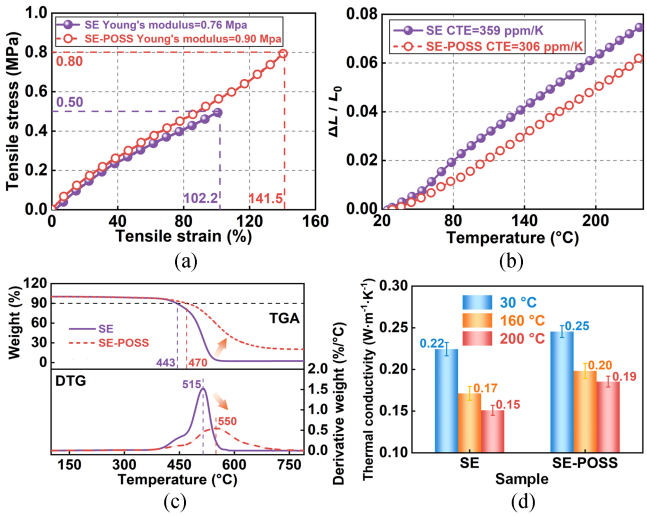

Fig. 3. (a) Tensile curve, (b) DMA curve, (c) TGA and DTG curve, and (d) thermal conductivity of SE and SE-POSS.

The thermal aging behaviors of SE include the side chain oxidation crosslinking and backbone cyclization degradation (see Fig. S20 and Note S15). The results indicate that the SE has more obvious degradation behavior than crosslinking behavior. However, the crosslinking behavior in the SE nanocomposites dominates, proving that the grafted POSS inhibits the polymer degradation and improves the antiaging ability of the strong crosslinking points around the POSS. Moreover, the SE-POSS 2wt% has the best anti-aging performance. Hence, it is deemed the optimal candidate for further study of thermal, mechanical, electrical, and module properties under high temperatures. Hereafter, the SE-POSS 2 wt% is labeled as SE-POSS.

B. Mechanical and Thermal Properties

Fig. 3(a) and (b) illustrates the tensile and DMA curves of SE and SE-POSS, respectively. Compared to SE, the tensile strength, tensile strain at break, and Young's modulus of SE-POSS are increased by 300 kPa, 39.3%, and 140 kPa, respectively. Furthermore, the dielectric spectrum analysis (see Fig. S21 and Note S16) indicates an increase in the ion hopping barrier and a denser, more compact molecular structure in SE-POSS. Fig. 3(b) demonstrates that SE-POSS has a lower CTE than SE. The measured hardness of SE and SE-POSS is 32 and 37 Shore A, respectively, with minimal susceptibility to thermal aging. Although the CTE of SE-POSS is higher than other hard components within the power modules, it does not pose serious thermo-mechanical stress due to its high softness. These results show that the movement and breakage of molecular segments are impeded, and the molecular interaction is enhanced in SE-POSS. This confirms the enhancement of mechanical properties in SE-POSS by incorporating grafted POSS nanofillers as localized mechanical reinforcement points.

Fig. 3(c) shows the TGA and DTG curves of SE and SE-POSS. The temperatures corresponding to the 90% weight loss and the fastest thermal decomposition of SE-POSS are higher than those of SE, indicating that SE-POSS exhibits superior thermal stability and a more resilient molecular structure, effectively impeding molecular cyclization degradation. Fig. 3(d) shows that the thermal conductivity of SE-POSS is higher than that of SE and decreases with temperature, suggesting that the molecular structure of SE-POSS is more orderly and uniform, resulting in improved phonon transfer and reduced phonon scattering.

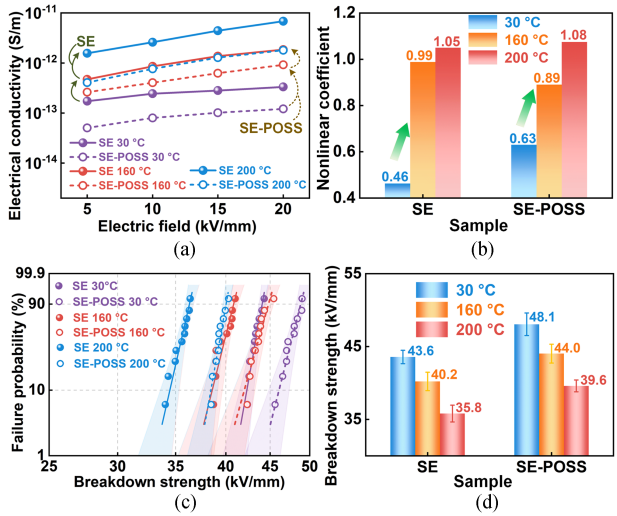

Fig. 4. (a) Electrical conductivity, (b) field-dependent nonlinear coefficient, (c) Weibull distributions of breakdown strength, and (d) characteristic breakdown strength of SE and SE-POSS at 30 °C, 160 °C, and 200 °C.

C. Electrical Properties

The electrical conductivities and their field-dependent nonlinear coefficients of SE and SE-POSS are depicted in Fig. 4(a) and (b), respectively. At the same temperature, SE-POSS exhibits a lower electrical conductivity than SE, and their conductivities, along with the nonlinear coefficients, increase as the temperature rises. Moreover, the electrical conductivity becomes directly proportional to the electric field at 200 °C, owing

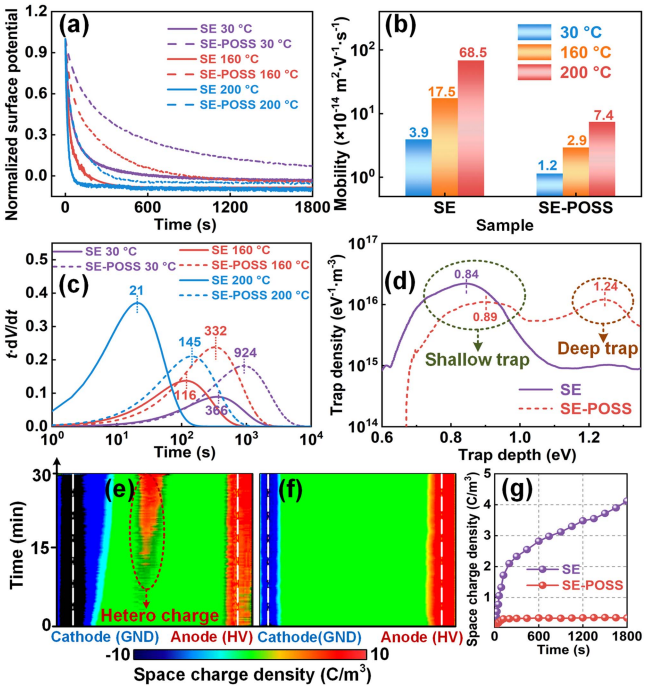

Fig. 5. (a) Normalized surface potential, (b) charge carrier mobility, (c) time for charge escaping from traps at 30 °C, 160 °C, and 200 °C; (d) trap distributions; space charge in (e) SE and (f) SE-POSS at 30 °C; (g) average space charge density for 30 min at 30 °C.

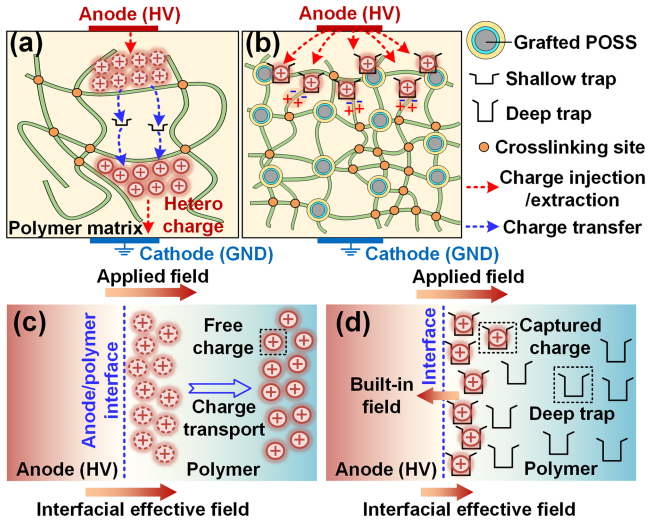

Fig. 6. Schematic diagram of charge transport in (a) SE and (b) SE-POSS; space-charge-modulated electric field at the anode/polymer interface in (c) SE and (d) SE-POSS.

to the nonlinear coefficient of approximately 1. Despite the positive correlation between the electrical conductivities of SE and SE-POSS with the electric field, their conductivities remain significantly lower than ceramic substrates under the same temperature. Consequently, their field-dependent conductivities have little impact on the electric field surrounding the triple point in the power modules (see Fig. S22). Hence, a lower electrical conductivity is preferred for SE nanocomposite to reduce its power loss.

The Weibull distributions of breakdown strengths and characteristic breakdown strengths of SE and SE-POSS are shown in Fig. 4(c) and (d), respectively. The SE-POSS has higher breakdown strength than SE at the same temperature, and their breakdown strengths decrease with temperature. The SE-POSS retains lower electrical conductivity and higher breakdown strength than SE even at the high temperature of 200 °C, indicating the grafted POSS nanofillers improve the high-temperature electrical properties in the SE-POSS.

D. Microscopic Charge Transport Properties

Fig. 5(a) and (b) presents the normalized SPD curves and charge carrier mobilities of SE and SE-POSS, respectively. The SPD curves of SE and SE-POSS are shown in Fig. S23, and their carrier mobilities are calculated by the transit time of SPD differential curves (see Fig. S24). SE-POSS demonstrates lower carrier mobility compared to SE at the same temperature, and both show an increase in carrier mobility with temperature, indicating enhanced charge migration as the temperature rises. Notably, the carrier mobilities of SE and SE-POSS exhibit a remarkable increase of 17.6 and 6.2 times, respectively, from 30 °C to 200 °C, showing that incorporating grafted nanofillers effectively impedes charge transport even at 200 °C.

The *y*-axis of Fig. 5(c) represents the time multiplied by the rate of potential decay, directly proportional to the quantity of de-trapped charges at a specific time (Note S5). Additionally, the peak value on the *y*-axis corresponds to the time required for most of the trapped charge to escape from the traps. Fig. 5(c) demonstrates that SE-POSS exhibits a longer charge escape time compared to SE at the same temperature, and this escape time diminishes as the temperature rises, suggesting that the trap depth in SE-POSS is greater than in SE, thereby making it more challenging for charges to escape from the traps. The trap distributions for both SE and SE-POSS are depicted in Fig. 5(d), derived from the TSDC curves (see Fig. S25). SE-POSS generates a large trap depth of 1.24 eV, and the shallow trap in SE-POSS also becomes deeper, increasing from 0.84 to 0.89 eV. Furthermore, Fig. 5(e) and (f) displays the space charge distributions of SE and SE-POSS under +10 kV/mm at 30 °C for 30 min, respectively. SE exhibits a significant accumulation of positive hetero space charges near the cathode, whereas no visible space charge is observed in the bulk of SE-POSS. The positive charges in SE are injected from the anode and migrate towards the cathode, creating hetero space charges. However, in SE-POSS, the charge injection and migration are hindered due to deeper traps introduced by POSS. Fig. 5(g) illustrates the continuous increase in average space charge density in SE, while it remains consistently low and stable in SE-POSS.

E. Microscopic Charge Transport Mechanism

Chemical impurities and structural flaws inevitably arise during the material production process of SE and SE-POSS, consequently leading to the development of localized energy levels within the cured material, commonly known as charge traps.

Fig. 6 depicts the schematics of the charge transport and space-charge-modulated electric field at the anode/polymer interface in SE and SE-POSS. In SE, a multitude of injected positive charges are frequently trapped and subsequently detrapped from shallow traps in the polymer matrix, migrating towards the cathode, thereby generating positive hetero space charge accumulation [see Fig. 6(a)]. The effective electric field at the anode/polymer interface remains as high as the applied field, resulting in further charge injection and transport [see Fig. 6(c)].

Conversely, the incorporation of grafted nanofillers in SE-POSS introduces deeper traps, rendering trapped charges more difficult to escape and forming a positive homo space charge layer in proximity to the anode [see Fig. 6(b)]. Notably, the deeply trapped positive homo charges diminish the effective field near the anode due to virtue of their built-in field opposing the applied field, thereby impeding subsequent charge injection and transport [see Fig. 6(d)]. Furthermore, the POSS grafting also leads to a more compact molecular structure and enhanced molecular interaction. If the injected charges become captured by the traps without de-trapping, space charge forms, rendering them unable to participate in charge transport. Consequently, deeper charge traps correspond to lower carrier mobility, reduced electrical conductivity, and increased breakdown strength.

IV. Module Testing

A. Electrical Tests of Lateral Modules

The encapsulated lateral modules are employed to examine the insulation properties of SE and SE-POSS as packaging materials under lateral electric stress. Fig. 7(a) displays the leakage currents of the lateral modules under DC +5 kV. Their electrical conductance, determined by the conduction current (Note S3), is presented in Fig. 7(b). The electrical conductance of the lateral module encapsulated with SE-POSS is significantly lower than that of SE, exhibiting a reduction of 59.8% at 200 °C. The Weibull distributions of ac PDIVs and rapid breakdown voltages are shown in Fig. S26. Fig. 7(c) and (d) reveals that SE-POSS exhibits higher PDIVs and rapid breakdown voltages compared to SE, demonstrating respective increases of 17.6% and 9.2% at 200 °C. This indicates the effective enhancement of leakage current reduction, PDIV, and breakdown voltage in the lateral modules at high temperatures by grafted POSS. The PDIV and breakdown voltage decrease with temperature, e.g., the PDIVs of SE and SE-POSS lateral modules are reduced by 35.2% and 29.8% from 30 °C to 200 °C, respectively, showing high temperatures deteriorate the packaging insulation.

The temporal variations of PD magnitude in the lateral modules during the IET growth process are depicted in Fig. 7(e). The PD magnitude in the lateral module of SE experiences rapid growth within the initial 100 s at 30 °C. However, the PD magnitudes of SE-POSS at 30 °C and 160 °C initially increase but subsequently decline to a consistently low level of around 100 pC. Moreover, the PD magnitude of SE shows an increasing trend at 200 °C, reaching over 2 nC at 300 s. Conversely, the PD magnitude of SE-POSS remains relatively stable, fluctuating within a narrow range around 1 nC. Fig. 7(f) illustrates the average PD density of the lateral modules during the IET growth process. The lateral module of SE-POSS displays lower PD density even at 200 °C.

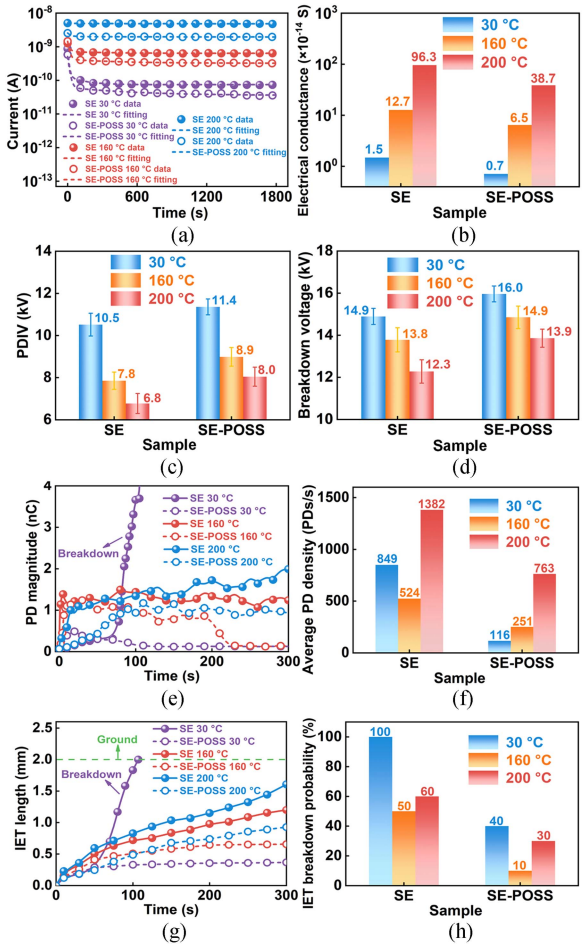

Fig. 7. (a) Leakage current, (b) electrical conductance, (c) PDIV, (d) breakdown voltage, (e) temporal variation of PD magnitude, (f) average PD density, (g) IET length, and (h) IET breakdown probability during the IET growth of lateral modules within 5 min at 30 °C, 160 °C, and 200 °C.

The IET length refers to the shortest distance between the end of the IET and the high-voltage copper trace. Fig. 7(g) shows that SE experiences rapid IET growth towards the ground copper trace at 30 °C, leading to IET breakdown. However, at 30 °C and 160 °C, the IET length of SE-POSS initially increases and subsequently stays constant. Additionally, the IET length of SE-POSS increases more slowly (less than 1 mm at 300 s) than SE at 200 °C. Notably, the IET grows more rapidly at higher temperatures in case of no IET breakdown. PD after the IET is initiated is the primary factor in IET development. By reducing PD magnitude and density, the grafted POSS decreases the IET growth rate, resulting in slow or stagnant IET growth in the lateral modules. Ten module samples are tested for the same temperature and material. Fig. 7(h) displays that SE-POSS has a significantly reduced IET breakdown probability as compared to SE due to the slower IET growth of SE-POSS.

The PRPD patterns of the lateral modules encapsulated with SE and SE-POSS during the final 30 s of IET growth at 200 °C are depicted in Fig. 8(a) and (b), respectively. Their IET morphology at 200 °C is shown in Fig. 8(c) and (d). The PRPD patterns

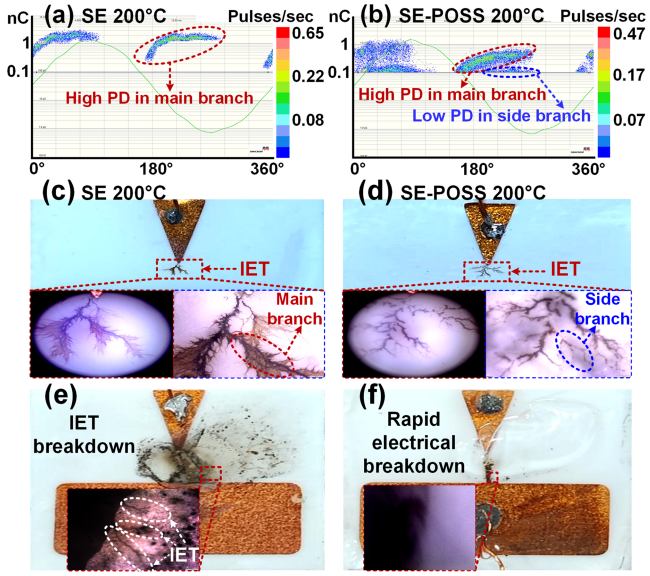

Fig. 8. PRPD patterns of the (a) SE and (b) SE-POSS lateral module at 200 °C; IET morphology in the (c) SE and (d) SE-POSS lateral module at 200 °C; (e) IET breakdown; (f) rapid electrical breakdown.

and IET morphology at 30 °C and 160 °C are presented in Fig. S27 and Fig. S28, respectively. The initiation of IET occurs at the sharp point of the high-voltage copper trace, intentionally designed as an electrical weak point with a highly concentrated electric field.

Fig. 8(a) illustrates that the PRPD pattern of the SE lateral module exhibits a "T" type distribution, characterized by predominantly high-amplitude PDs with the absence of low-amplitude PDs, indicative of tip discharge phenomena. The high-amplitude PDs usually occur in the thick main branches, while the low-amplitude PDs are dispersed across the thinner side branches, growing from the side of the main branches. The growth of IET in the SE lateral module is primarily accompanied by the high-amplitude PDs [see Fig. 8(a)], leading to the concentration of energy in the main branches, resulting in their thickening and the inhibition of side branch growth [see Fig. 8(c)]. The high-energy main branches propagate rapidly within the SE lateral module, easily leading to IET breakdown.

Fig. 8(b) demonstrates that numerous low-amplitude PDs emerge in the SE-POSS lateral module while the magnitude of high-amplitude PDs decreases, resulting in the formation of more side branches in the IET [see Fig. 8(d)], dispersing the energy from the main branches. The IET main branches in SE-POSS also become shorter and thinner than SE (see Fig. S29). Hence, the propagation of the main branches becomes slow or even stagnant, and the IET ends consist of side branches instead of main branches. The reduced PD magnitudes in SE-POSS at 30 °C and 160 °C further indicate the transfer of PD from the main branches to the side branches, stagnating the growth of the main branches and forming more expanding side branches. Hence, the IET in SE-POSS becomes denser with time rather than longer, and its growth is hindered. Additionally, the IET branch becomes thicker and darker, and more main branches appear as the temperature increases (see Fig. S29).

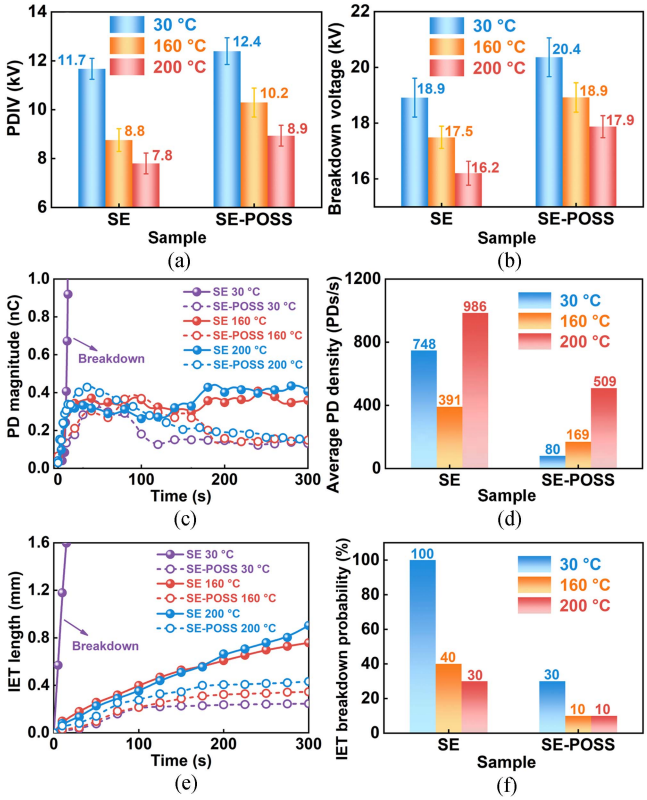

Fig. 9. (a) PDIV, (b) rapid breakdown voltage, (c) temporal variation of PD magnitude, (d) average PD density, (e) IET length, and (f) IET breakdown probability during the IET growth of vertical modules within 5 min at 30 °C, 160 °C, and 200 °C.

Notably, the PD at the phase of 0° and 180° is observed at both SE and SE-POSS, indicating that the PD is determined by the composite electric field formed by the external electric field and the space charge around the IET. The PD behaviors at 0° and 180° are modulated by the built-in electric field formed by space charge during the IET growth.

Fig. 8(e) and (f) illustrates IET breakdown and rapid electrical breakdown in the lateral modules, respectively. Some IET branches exist around the main IET breakdown channel, and parts of its surface appear hollow and transparent, whereas the rapid electrical breakdown channel is straighter without curvature, and no IET branches are observed around it. Moreover, compared to the rapid electrical breakdown, the IET breakdown occurs at a much lower voltage [see Fig. 7(c) and (d)] and takes longer. Therefore, the IET should be considered separately from the rapid electrical breakdown in designing the packaging insulation in the power modules.

B. Electrical Tests of Vertical Modules

The encapsulated vertical modules are employed to study the insulation characteristics of SE and SE-POSS as packaging materials under vertical ac electric stress. Fig. S30 shows the Weibull distributions of PDIVs and rapid breakdown voltages. Fig. 9(a) and (b) displays the PDIVs and rapid breakdown voltages of the SE and SE-POSS vertical modules at 30 °C, 160 °C, and 200 °C. The SE-POSS exhibits higher PDIV and

rapid breakdown voltage values than SE, showcasing respective enhancements of 14.1% and 10.5% at 200 °C. The PDIVs of SE and SE-POSS vertical modules are reduced by 33.3% and 28.2% from 30 °C to 200 °C, respectively. Furthermore, the PDIV or breakdown voltage in the vertical module surpasses that in the lateral module owing to the lower electric field around the triple point in the vertical module than the lateral module subjected to the same voltage (see Fig. S8 and Fig. S10).

Fig. 9(c) illustrates the temporal variations of PD magnitude within the SE and SE-POSS vertical modules during the IET growth process. The PD magnitude within the SE vertical module exhibits a rapid surge at 30 °C. Moreover, the PD magnitudes within the SE vertical module at 160 °C and 200 °C rise and maintain stability at an elevated level of around 400 pC. Notably, the PD magnitudes in the SE-POSS vertical module escalate to a higher amplitude initially, gradually diminishing to a relatively lower amplitude of around 150 pC after 300 s under 30 °C, 160 °C, and 200 °C. Fig. 9(d) shows that the average PD density of SE-POSS is comparatively lower than that of SE at equivalent temperatures, progressively increasing with the rise in temperature. These outcomes prove that the grafted POSS enhances the PDIV and breakdown voltage while reducing the PD magnitude and density in the vertical modules.

Fig. 9(e) shows that the IET length of SE grows significantly at 30 °C, which causes IET breakdown. At 160 °C and 200 °C, the IET of SE is constantly growing. However, the IET lengths of SE-POSS at 30 °C, 160 °C, and 200 °C initially increase and then stabilize less than 0.5 mm. Besides, in the absence of IET breakdown, the IET grows more rapidly with rising temperatures. Fig. 9(f) shows that SE-POSS has a lower IET breakdown probability than SE. This suggests that the grafted POSS can hinder the IET growth and lessen the likelihood of IET breakdown. The IET breakdown probabilities of both SE and SE-POSS modules at 30 °C surpass those at 160 °C and 200 °C. This is attributed to the notably higher voltage triggering IET, owing to the higher PDIV at 30 °C. In SE modules, higher electric field energy concentrates in IET main branches under elevated voltages, rapidly evolving IET until breakdown in a short time across all modules. However, in SE-POSS modules, the dense nanostructure disperses high energy from the main branches into numerous low-energy side branches, inhibiting IET growth and reducing the likelihood of breakdown.

Fig. 10(a) and (b) illustrates the PRPD patterns within the vertical modules of SE and SE-POSS, respectively, during the final 30-s interval of the IET growth at 200 °C. Their respective IET morphology at 200 °C is visualized in Fig. 10(c) and (d), while the PRPD patterns and IET morphology at 30 °C and 160 °C are presented in Fig. S31 and Fig. S32, respectively. The IET is initiated from the stochastic metal protrusions along the upper copper edge.

Fig. 10(a) showcases a "Γ"-type PRPD pattern in the SE vertical modules, characterized by numerous high-amplitude PDs. In contrast, Fig. 10(b) exclusively exhibits occurrences of low-amplitude PDs in SE-POSS. Fig. 10(c) depicts the emergence of thick main branches that extend along the direction of the electric field in SE, whereas Fig. 10(d) shows a higher prevalence of slender side branches near the IET end and the copper edge in

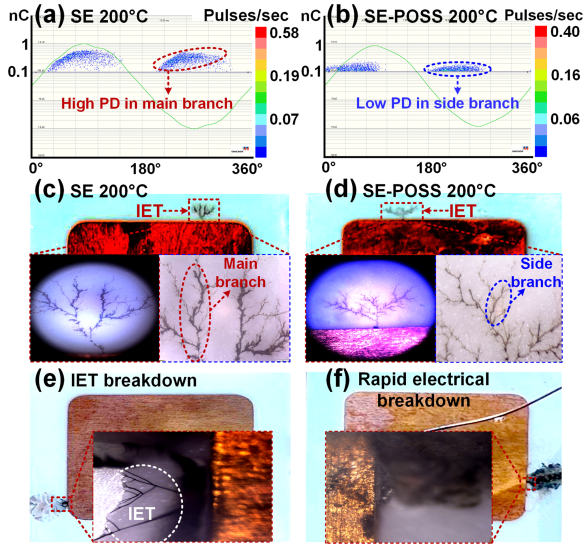

Fig. 10. PRPD patterns of the (a) SE and (b) SE-POSS vertical module at 200 °C; IET morphology in the (c) SE and (d) SE-POSS vertical module at 200 °C; (e) IET breakdown; (f) rapid electrical breakdown.

SE-POSS. Besides, the IET branches in SE-POSS also exhibit a more slender, shorter, and denser structure than SE (see Fig. S33). These results indicate that the grafted POSS diminishes the concentrated energy in the sparsely distributed IET main branches with high PD magnitude and density. Consequently, a greater portion of energy is dissipated through low-amplitude and low-density PDs in the denser side branches. The formation and expansion of more side branches further exacerbate energy dispersion, and the denser side branches with lower energy grow slowly or stagnate, impeding the propagation of the main branch, and resulting in the deceleration and stagnation of the insulation degradation.

Fig. 10(e) and (f) illustrates the IET breakdown and rapid electrical breakdown in the vertical modules, respectively. Notably, the IET breakdown channel manifests the emergence of certain IET branches in its proximity, while no observable IET branches are discerned during rapid electrical breakdown. Furthermore, the rapid electrical breakdown channel is thicker and darker than the IET breakdown channel.

C. *Space-Charge-Modulated IET Growth Mechanism*

Fig. 11 illustrates the mechanisms of the charge transport and space-charge-modulated IET growth in the SE and SE-POSS modules. Through electrical, thermal, and mechanical experiments reported in Section III, SE-POSS exhibits lower carrier mobility and higher molecular strength than SE. In SE, a multitude of high-energy free charges are injected from the random copper protrusions and swiftly migrate along the direction of the applied electric field towards the opposite electrode [see Fig. 11(a)], leading to the disruption of the molecular structure via impact ionization, consequently forming the main branches of IET. The accumulated hetero space charges near the copper protrusion increase its electric field and enhance the injection of the high-energy charges. With the gradually

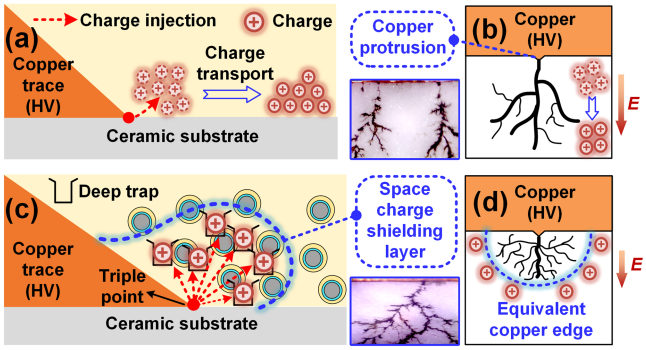

Fig. 11. (a) Charge transport in SE, (b) space-charge-modulated IET growth in SE; (c) charge transport in SE-POSS, (d) space-charge-modulated IET growth in SE-POSS.

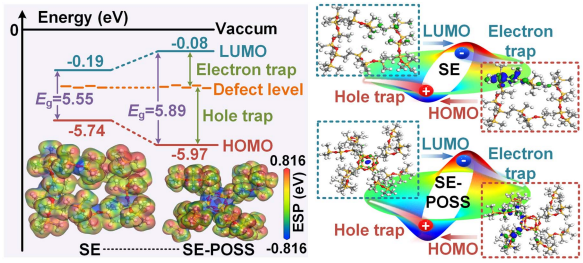

Fig. 12. (a) HOMO, LUMO, energy bandgap, and ESP. (b) Charge trapping process in SE and SE-POSS.

accumulated collisions of these high-energy charges, the IET main branches undergo thickening and rapid growth until the ultimate breakdown of the packaging modules [see Fig. 11(b)].

In SE-POSS, the injected charges with low carrier mobility are quickly captured by the deep traps near the electrode, thereby creating a homo space charge shielding layer and reducing the electric field in the vicinity of the copper protrusion [see Fig. 11(c)]. As a result, the number and energy of the injected charges decrease, incapable of causing significant damage to the molecular structure and forming main branches. These low-energy charges generate dense slender side branches within the uniform electric field around the copper protrusion. Furthermore, these charges disperse further along the side branches, leading to a wider distribution of space charges, enhancing their uniform effect on the electric field. Additionally, the ends of the side branches create an equivalent copper edge with a larger curvature radius in comparison to the copper protrusion due to the space charge shielding effect [see Fig. 11(d)]. In the case of a few un-trapped free charges, the dense side branches facilitate charge dispersion, preventing the accumulation of free charges and the subsequent destruction of molecular chains caused by a substantial influx of charges. The limited number of low-energy free charges in the side branches is insufficient to sustain IET growth, impeding further IET propagation.

Furthermore, the augmented mechanical properties of SE-POSS compared to SE signify an enhancement in the molecular interaction and strength. The reinforced molecular structure makes it difficult to be destroyed by the high-energy free charges and likewise impedes the growth of the IET. Consequently, it can be considered that lower charge mobility could mitigate the destructive impact of injected charges on the material, and bolstering the molecular interaction could heighten the material's resistance against the charge collision. Therefore, minimizing the charge carrier mobility and enhancing the molecular interaction is imperative to improve PDIV and impede IET propagation.

V. Material and Module Simulations

A. Quantum Chemical Calculation of Molecular Structure

To verify the optimized molecular properties and obtain the microscopic mechanism of lower carrier mobility in SE-POSS, the molecular energy level distributions, molecular binding energy, electrostatic potential (ESP), and deformation charge density of SE and SE-POSS are acquired by quantum chemical calculations based on density functional theory (DFT). The simplified molecular models of SE and SE-POSS are displayed in Fig. S34, and the calculation details are outlined in Note S17. The LUMO and HOMO are the lowest unoccupied molecular orbital and the highest occupied molecular orbital, respectively. The electrons and holes can move freely on the LUMO and HOMO, respectively. The density of electron states, LUMO, and HOMO of SE and SE-POSS are presented in Fig. S35. Fig. 12(a) shows that the LUMO increases while the HOMO decreases in SE-POSS, consequently resulting in a larger energy bandgap (E_g). This augmented energy bandgap heightens the trap depth within SE-POSS, leading to lower carrier mobility. The molecular binding energy of SE and SE-POSS is 8013 and 14229 Ha, respectively, indicating that SE-POSS has a more compact molecular structure and enhanced molecular electrostatic interaction than SE.

To further ascertain the origins of the deep traps in SE-POSS, the deformation charge density and ESP are depicted in Fig. S36 and Fig. 12(a), respectively. Fig. S36 demonstrates that the oxygen atoms function as electron traps by acquiring electrons, while the silicon atoms serve as hole traps by losing electrons. The trap distribution is dispersed along the SE molecular chain, whereas the grafted POSS imparts a dense distribution of oxygen and silicon atoms, resulting in deep traps being concentrated within the POSS. The ESP of SE-POSS in Fig. 12(a) displays a negatively charged profile of the POSS, enabling it to capture holes, while the center of the POSS is positively charged, facilitating the capture of electrons. Hence, the grafted POSS provides deeper charge traps. Fig. 12(b) illustrates the process of electron and hole trapping in SE and SE-POSS. The electrons on the LUMO and the holes on the HOMO become captured by deeper traps in SE-POSS, making it arduous for them to escape and migrate.

B. BCT Simulation of Packaging Module

To verify the restraining effect of deeper traps and lower charge carrier mobility on charge transport in the packaging insulation, the BCT model (Note S18) is established to simulate charge transport and space-charge-modulated electric field within the SE and SE-POSS packaging modules for 30 min

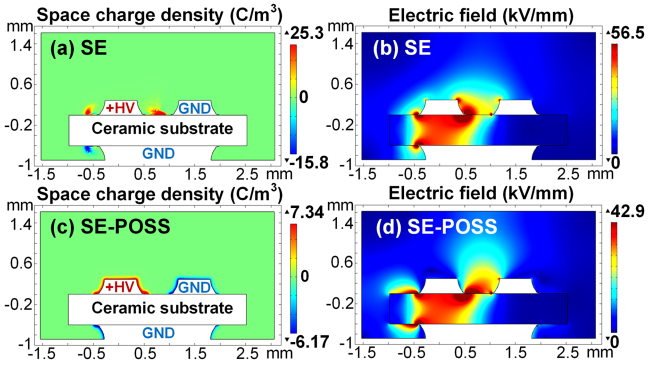

Fig. 13. (a) Space charge and (b) electric field distribution in SE packaging module; (c) space charge and (d) electric field distribution in SE-POSS packaging module. (The simulation duration is 30 min and the temperature is set to 200 °C.)

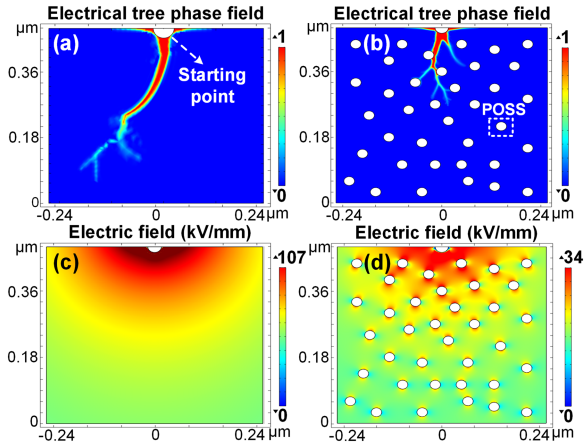

Fig. 14. Phase field simulation of the electrical tree in (a) SE and (b) SE-POSS at 200 s; the simulated electric field distributions in (c) SE and (d) SE-POSS at 0 s.

at 200 °C. The trap depths for SE and SE-POSS are 0.84 and 1.24 eV, and the carrier mobilities of SE and SE-POSS are 6.85×10^{-13} and 7.4×10^{-14} $m^2/(V \cdot s)$, respectively, from the microscopic charge transport properties. The structural model of the packaging module is depicted in Fig. S37, whereby the left copper trace is subjected to DC +5 kV to ensure the long-term effect of the constant electric field on charge transport, while the right and bottom copper traces are grounded. Fig. 13 displays the distributions of space charge and electric field within the SE and SE-POSS packaging modules.

Fig. 13(a) reveals that a multitude of positive charges within the SE module are injected from the left HV copper trace and migrate towards the right ground copper trace along the packaging material/ceramic substrate interface, resulting in the buildup of hetero space charges near the ground copper trace. The maximum density of this accumulated space charge is measured at 25.3 C/m^3. Conversely, Fig. 13(c) illustrates that the homo charge accumulates at the surface of the copper traces in the SE-POSS module, forming a thin layer of homo space charges, and the maximum space charge density amounts to only 7.34 C/m^3. This is consistent with the space charge results for SE and SE-POSS in Fig. 5(e) and (f). Fig. 13(b) and (d) demonstrates that the maximum electric fields at the triple point within the SE and SE-POSS modules are 56.5 and 42.9 kV/mm, respectively. These outcomes indicate that the deeper traps and reduced carrier mobility in SE-POSS impede the injection and migration of charges within the packaging modules, thereby alleviating the electric field around the triple point.

C. Phase Field Simulation of the Electrical Tree in Material

The phase field simulation of the electrical tree (Note S19) is used to study the barrier effect of the grafted POSS on the electrical tree growth, and the geometrical model is shown in Fig. S38. Simulations employ the needle-plane electrodes, with the shortest distance between the needle tip and ground plane set at 0.8 μm. The electrical tree starting point was set at the top-middle position of the simulation domain, and the high-voltage needle electrode was applied with ac 100 V, creating an electric field over 150 kV/mm around the needle tip. The simulation results of the electrical tree and electric field in SE and SE-POSS are shown in Fig. 14.

Fig. 14(a) and (b) demonstrates that, compared to the electrical tree observed in SE at 200 s, the electrical tree in SE-POSS is characterized by a shorter length and several slender side branches. These branches extend towards the grafted POSS, but their growth is impeded upon encountering the POSS due to the physical barrier effect of the POSS. It indicates that the presence of side branches in the SE-POSS causes a higher energy dissipation than a straight path without branches in SE, thereby reducing the propagation velocity of the electrical tree.

Fig. 14(c) and (d) illustrates that a concentrated electric field occurs around the starting point in SE at 0 s, reaching a maximum value of 107 kV/mm. However, the presence of grafted POSS leads to a reduction and homogenization in the high electric field around the starting point in SE-POSS, and the maximum electric field is reduced to 34 kV/mm. The resulting homogeneity of the electric field contributes to forming more side branches, impeding the elongation of the electrical tree.

D. Phase Field Simulation of the IET in Packaging Module

The lower microscopic charge carrier mobility corresponds to the lower macroscopic electrical conductivity. To investigate the inhibitory effect of the reduced electrical conductivity on the IET growth in the packaging modules, the phase field model is used for the first time in the IET simulations of the packaging modules (Note S20). The packaging insulation material is supposed to be homogeneous, and only the electrical conductivity is varied. The high-voltage copper trace is applied to an ac voltage of 10 kV, and the starting point is set 1 μm far from the sharp point of the copper trace to weaken the effect of grid meshing on the simulation results. The side views of the IET phase field in the packaging insulation with the electrical conductivity of 10^{-15} S/m and 10^{-14} S/m at 10 s are shown in Fig. 15. The IET has a shorter length in the packaging insulation with the electrical conductivity of 10^{-15} S/m than the packaging insulation with an electrical conductivity of 10^{-14} S/m, proving the packaging

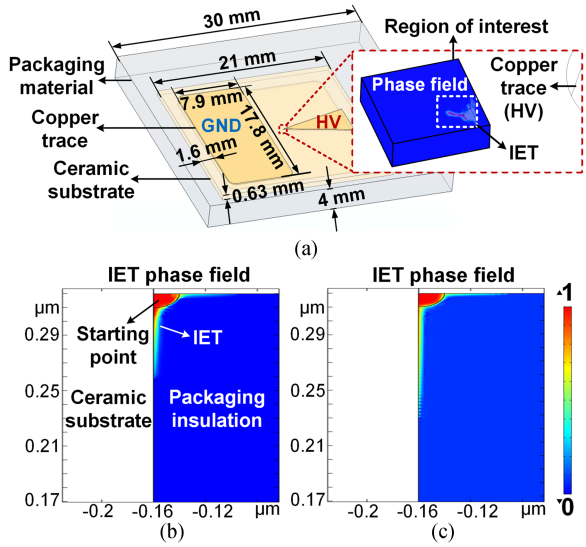

Fig. 15. (a) Phase-field simulation of the IET in the lateral module; the IET in the packaging insulation with the electrical conductivity of (b) 10^{-15} S/m and (c) 10^{-14} S/m at 10 s.

insulation with lower carrier mobility and a lower electrical conductivity can impede the IET growth effectively.

The aforementioned module-based IET simulation method is recommended for industrial applications in high-temperature packaging insulation design. Its utility lies in identifying weaknesses in module design and potential locations for IET propagation in the packaging insulation. The method holds promise in providing significant insights for the high-temperature IET-resistant design of packaging insulation materials.

Furthermore, the IET growth under ac voltages is affected by both the electric field energy and the Joule heat energy. The electric field energy is determined by the electric field and the permittivity of the packaging insulation, while the Joule heat energy is contingent upon the electric field and the packaging insulation's electrical conductivity. In this study, the primary objective is to investigate the impact of the Joule heat energy resulting from the insulation's electrical conductivity on the IET growth. Due to the dependency of the ac electric fields on the applied voltage and the packaging insulation's permittivity and considering the slight effect of POSS grafting on the SE's permittivity, the applied voltage and the packaging insulation's permittivity are kept constant to maintain a consistent electric field energy. Only variation in the electrical conductivity is employed to modify the Joule heat energy. This ensures that the electrical conductivity is the only factor affecting the IET.

Therefore, when employing module-based IET simulation in the complex industrial design of high-temperature packaging insulation, it is imperative to concurrently consider the effects of applied voltages, permittivity, and electrical conductivity of the packaging insulation on the IET growth within the power modules. Altering the packaging insulation's permittivity or applied voltage results in variations in the electric fields with the power modules, simultaneously affecting both the electric field energy and Joule heat energy within the insulation, thereby leading to a more intricate impact on the IET.

VI. High-Temperature IET-Resistant Packaging Insulation Design Procedure

The inception of the IET in packaging modules occurs at a substantially lower voltage than their breakdown voltage, and it takes a longer time to progress towards ultimate breakdown. Furthermore, the IET is triggered at a lower voltage and exhibits faster propagation with increasing temperature. While the PD of a new power module is not detected within a short duration by the manufacturer, the IET may unexpectedly emerge during prolonged operation under rated electrical stress, especially for the SiC modules operating at temperatures exceeding 175°C. Timely detection of the IET proves challenging as power modules continue to function normally during IET initiation and growth stages. Nonetheless, if the triggered IET remains undetected or unaddressed, it can ultimately result in complete module failure. Moreover, preventing the initiation of the IET is a complex task due to the unresolved issues concerning the concentrated electric field around the triple points and an unexpectedly high electric field near random copper protrusions in the current manufacturing processes of power modules. These issues cause continuous electrical aging of the packaging insulation, fostering the IET initiation and growth.

Furthermore, the existing design of the high-temperature packaging insulation primarily focuses on enhancing thermal stability, bolstering breakdown strength, and attaining higher short-time PDIV. However, little attention has been directed towards the phenomenon of IET and IET-resistance design within the packaging insulation. Therefore, the IET should be considered separately from electrical breakdown, and the packaging insulation design should not limit its focus solely to thermal stability and breakdown strength. Instead, equal consideration must be given to enhancing high-temperature IET resistance. In the case of IET initiation, its propagation should be effectively inhibited, ensuring slower or even stagnant growth, which can provide extended operational windows for power modules, allowing for prolonged usage and facilitating diagnosis. A novel high-temperature IET-resistant packaging insulation design procedure is proposed in Fig. 16.

Drawing upon the preceding experimental and simulation work, this study proposes two IET-resistant design principles, covering both macroscopic and microscopic levels, considering the modulation effect exerted by space charges on the growth of IET. The macroscopic aspects especially include reducing electrical conductivity and augmenting mechanical strength, while the microscopic facets encompass decreasing charge carrier mobility and enhancing molecular interaction.

The design procedure for achieving high-temperature IET resistance in packaging insulation is outlined as follows:

Step 1. Design IET-resistant packaging insulation

Nano or subnano fillers are preferred in the IET-resistance design owing to their barrier effect against IET growth. These fillers can hinder charge transport by introducing deep traps and simultaneously enhancing molecular interactions by their

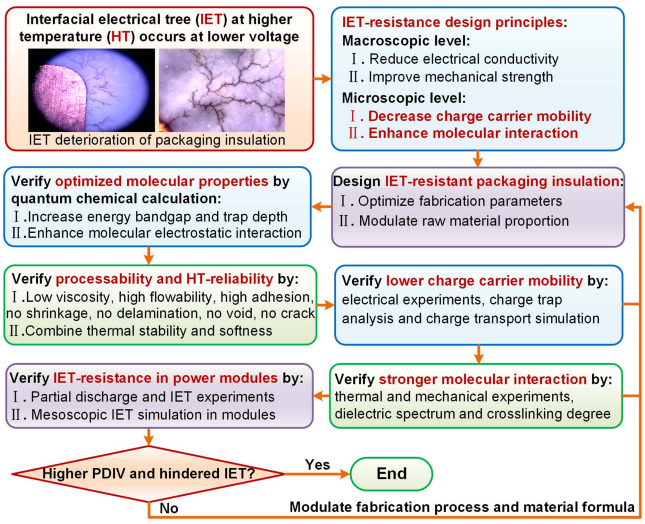

Fig. 16. High-temperature IET-resistant packaging insulation design principles and procedure.

interfacial effect. Moreover, ensuring the uniform dispersion of these fillers and their high compatibility with the polymer matrix is paramount in achieving optimal IET resistance. However, conventional methods for dispersing fillers, such as mechanical stirring and ultrasonic dispersion, are expensive, time-consuming, and prone to causing filler aggregation. Therefore, an innovative grafting technique of nanofillers is proposed for their effective dispersion within the matrix.

Step 2. Verify optimized molecular properties

After establishing an initial material composition and optimizing the molecular structure subsequently, the molecular properties, including energy levels of molecular orbitals, binding energy, ESP, and charge density, are acquired through quantum chemical calculations employing DFT. To validate the presence of deeper charge traps and augmented molecular electrostatic interaction, it is imperative that the energy bandgap and molecular binding energy of the optimized molecular structure surpass those achieved in the previous round of material optimization.

Step 3. Verify processability and HT-reliability

The raw materials used for packaging insulation should exhibit low viscosity, slow curing, and high flowability to fill the intricate module structure effectively. Once cured, the packaging insulation must exhibit strong adhesion to other components and maintain low residual internal stress without volume shrinkage, voids, bubbles, or crosslinking byproducts. Even under high-temperature thermal aging, there should be no interface delamination in the modules or surface cracks exposed to oxygen. Besides, high-temperature reliability should tradeoff between thermal stability and softness. The high-temperature packaging material should possess appropriate elastic modulus and CTE, ensuring it does not cause serious thermo-mechanical stress to other components in the power modules, maintaining high packaging reliability under high temperatures.

Step 4. Verify lower charge carrier mobility

Upon validating the optimized molecular properties, the packaging insulation material should be further examined by a series of electrical experiments, including electrical conductivity, breakdown strength, space charge, TSDC, and SPD. By conducting these electrical tests, it is plausible to ascertain and substantiate the presence of deeper charge traps and lower charge carrier mobility. To validate the impeded charge transport within the packaging modules, the utilization of the BCT model becomes necessary.

Step 5. Verify stronger molecular interaction

After verifying the lower charge carrier mobility, the packaging material should exhibit higher thermal stability, higher mechanical strength, and lower CTE by the thermal and mechanical experiments to verify the stronger molecular interaction. The inhibited molecular relaxation movement at high temperatures can be verified by the dielectric spectrum. Besides, a more resilient molecular structure can also be verified by the crosslinking degree measurement.

Step 6. Verify IET-resistance in power modules

Finally, the insulation material with lower carrier mobility and enhanced molecular interaction should be encapsulated in the packaging modules, and a higher PDIV and hindered IET should be verified in the packaging modules encapsulated with the new material. Besides, the inhibition effect of the new material on the IET growth in the power modules can also be verified by the mesoscopic phase field simulation. If any of the above steps fails, the design procedure should return to Step 1, and the material's fabrication process and raw material formula should be modulated. The next round of optimization should continue until it passes the verification.

VII. Conclusion

The IET-resistant design is not considered in the current high-temperature packaging insulation design. A novel low-content POSS-grafted SE nanocomposite is proposed, and its electrical, thermal, mechanical, and aging properties are explored. The IET-resistance performance and its accompanying PD characteristics of the grafted nanocomposite in the lateral and vertical packaging modules are investigated at low and high temperatures. Moreover, the microscopic charge transport mechanism in the material and the space-charge-modulated IET growth mechanism in the module are revealed. Combined with the experimental and simulation results, the design principles and procedure for high-temperature IET-resistant packaging insulation are proposed.

1) The proposed nano-POSS grafting technique can achieve high dispersion and high compatibility of nanofillers at an extremely low doping level, avoiding the shortcomings of traditional filler doping processes. The grafted nanocomposite exhibits lower mass loss and retains better electrical properties after thermal aging. Compared to the ungrafted material, the grafted material has better mechanical strength and thermal stability, lower electrical conductivity, and higher dielectric strength at high temperatures. The grafted POSS reduces the charge carrier mobility by

introducing deeper traps, inhibiting charge transport in the grafted nanocomposite.

2) Whether it is a lateral or vertical module, the grafted packaging insulation has higher PDIV and breakdown voltage and lower PD magnitude and density. The IET structure of the grafted nanocomposite is shorter, denser, and slenderer, and the IET pattern transits from the rapid growth of high-PD main branches in the ungrafted material to the slow growth or even stagnation of low-PD side branches in the grafted material. Deep traps in the grafted material capture injected charges and form a space charge layer to homogenize the electric field near the triple point. The IET energy in the grafted material is dispersed by dense low-energy side branches at the end of IET and near the copper protrusion, inhibiting the IET growth and reducing the IET breakdown probability. The PDIV decreases, and the IET grows faster at higher temperatures.
3) The packaging insulation with a larger energy bandgap and molecular energy can introduce deeper charge traps and enhance molecular interactions. The packaging insulation with lower carrier mobility can suppress charge transport and IET growth in the packaging modules. The design criteria and procedure of the IET-resistant packaging insulation material are proposed to facilitate the packaging insulation design of the high-temperature power modules, combining the quantum chemical calculations of materials, BCT simulation, and IET phase-field simulations of modules.

ACKNOWLEDGMENT

Qilong Wang would like to thank the technical support from Mr. Huiqiang Yan of the College of Electrical Engineering, Zhejiang University.

REFERENCES

[1] L. Zhang, X. Yuan, X. Wu, C. Shi, J. Zhang, and Y. Zhang, "Performance evaluation of high-power SiC MOSFET modules in comparison to Si IGBT modules," *IEEE Trans. Power Electron.*, vol. 34, no. 2, pp. 1181–1196, Feb. 2019.

[2] M. Sato, A. Kumada, K. Hidaka, K. Yamashiro, Y. Hayase, and T. Takano, "Surface discharges in silicone gel on AlN substrate," *IEEE Trans. Dielectrics Elect. Insul.*, vol. 23, no. 1, pp. 494–500, Feb. 2016.

[3] Y. Yao, G.-Q. Lu, D. Boroyevich, and K. D. T. Ngo, "Survey of high-temperature polymeric encapsulants for power electronics packaging," *IEEE Trans. Compon., Packag. Manuf. Technol.*, vol. 5, no. 2, pp. 168–181, Feb. 2015.

[4] R. Khazaka, L. Mendizabal, D. Henry, and R. Hanna, "Survey of high-temperature reliability of power electronics packaging components," *IEEE Trans. Power Electron.*, vol. 30, no. 5, pp. 2456–2464, May 2015.

[5] B. Zhang, M. Ghassemi, and Y. Zhang, "Insulation materials and systems for power electronics modules: A review identifying challenges and future research needs," *IEEE Trans. Dielectrics Elect. Insul.*, vol. 28, no. 1, pp. 290–302, Feb. 2021.

[6] M. Sato, A. Kumada, K. Hidaka, K. Yamashiro, Y. Hayase, and T. Takano, "Dynamic potential distributions of surface discharge in silicone gel," *IEEE Trans. Dielectrics Elect. Insul.*, vol. 22, no. 3, pp. 1733–1738, Jun. 2015.

[7] S. Nakamura et al., "Electrical treeing in silicone gel under repetitive voltage impulses," *IEEE Trans. Dielectrics Elect. Insul.*, vol. 26, no. 6, pp. 1919–1925, Dec. 2019.

[8] P. Mancinelli, A. Cavallini, S. J. Dodd, N. M. Chalashkanov, and L. A. Dissado, "Analysis of electrical tree inception in silicone gels," *IEEE Trans. Dielectrics Elect. Insul.*, vol. 24, no. 6, pp. 3974–3984, Dec. 2017.

[9] T. M. Do, O. Lesaint, and J.-L. Auge, "Streamers and partial discharge mechanisms in silicone gel under impulse and AC voltages," *IEEE Trans. Dielectrics Elect. Insul.*, vol. 15, no. 6, pp. 1526–1534, Dec. 2008.

[10] L. Wang, Z. Zeng, P. Sun, S. Ai, J. Zhang, and Y. Wang, "Electric-field-dominated partial discharge in medium voltage SiC power module packaging: Model, mechanism, reshaping, and assessment," *IEEE Trans. Power Electron.*, vol. 37, no. 5, pp. 5422–5432, May 2022.

[11] Z. Zhang, K. D. T. Ngo, and G.-Q. Lu, "Characterization of a nonlinear resistive polymer-nanoparticle composite coating for electric field reduction in a medium-voltage power module," *IEEE Trans. Power Electron.*, vol. 37, no. 3, pp. 2475–2479, Mar. 2022.

[12] Z. Zhang et al.., "Packaging of a 10-kV double-side cooled silicon carbide diode module with thin substrates coated by a nonlinear resistive polymer-nanoparticle composite," *IEEE Trans. Power Electron.*, vol. 37, no. 12, pp. 14462–14470, Dec. 2022.

[13] M. M. Tousi and M. Ghassemi, "Characterization of nonlinear field-dependent conductivity layer coupled with protruding substrate to address high electric field issue within high-voltage high-density wide bandgap power modules," *IEEE J. Emerg. Sel. Topics Power Electron.*, vol. 8, no. 1, pp. 343–350, Mar. 2020.

[14] S. Nakamura et al., "Effects of temperature on electrical treeing and partial discharges in epoxy/silica nanocomposites," *IEEE Trans. Dielectrics Elect. Insul.*, vol. 27, no. 4, pp. 1169–1177, Aug. 2020.

[15] X. Zhu, J. Wu, Y. Wang, and Y. Yin, "Characteristics of partial discharge and AC electrical tree in XLPE and MgO/XLPE nanocomposites," *IEEE Trans. Dielectrics Elect. Insul.*, vol. 27, no. 2, pp. 450–458, Apr. 2020.

[16] B. X. Du, Y. M. Li, C. L. Han, T. Han, and Z. L. Li, "Graphene nanoplatelets and temperature gradient affecting electrical tree in Graphene/SiR nanocomposites," *IEEE Trans. Dielectrics Elect. Insul.*, vol. 28, no. 4, pp. 1255–1263, Aug. 2021.

[17] Y. Wang, J. Wu, Y. Yin, and T. Han, "Effect of micro and nano-size boron nitride and silicon carbide on thermal properties and partial discharge resistance of silicone elastomer composite," *IEEE Trans. Dielectrics Elect. Insul.*, vol. 27, no. 2, pp. 377–385, Apr. 2020.

[18] Y. Y. Yao et al., "Effect of Al_2O_3 fibers on the high-temperature stability of silicone elastomer," *Polymer*, vol. 55, no. 16, pp. 4232–4240, 2014.

[19] Y. Y. Yao et al., "Dielectric strength of Al_2O_3/silicone composites after high-temperature aging," *J. Appl. Polym. Sci.*, vol. 131, no. 23, 2014, Art. no. 41170.

[20] M.-L. Locatelli et al., "Evaluation of encapsulation materials for high-temperature power device packaging," *IEEE Trans. Power Electron.*, vol. 29, no. 5, pp. 2281–2288, May 2014.

[21] X. Chen, Q. Wang, N. Ren, C. Dai, M. Awais, and A. Paramane, "Potential of epoxy nanocomposites for packaging materials of high voltage power modules: A validation using experiments and simulation," *IEEE Trans. Dielectrics Elect. Insul.*, vol. 28, no. 6, pp. 2161–2169, Dec. 2021.

[22] J. Y. Xu et al., "Trap characteristics and their temperature-dependence of silicone gel for encapsulation in IGBT power modules," *Chin. Soc. Elect. Eng. J. Power Energy Syst.*, vol. 7, no. 3, pp. 614–621, 2021.

[23] Z. Chen, Y. Yao, D. Boroyevich, K. D. T. Ngo, P. Mattavelli, and K. Rajashekara, "A 1200-V, 60-A SiC MOSFET multichip phase-leg module for high-temperature, high-frequency applications," *IEEE Trans. Power Electron.*, vol. 29, no. 5, pp. 2307–2320, May 2014.

[24] Y. Yao, Z. Chen, G.-Q. Lu, D. Boroyevich, and K. D. T. Ngo, "Characterization of encapsulants for high-voltage high-temperature power electronic packaging," *IEEE Trans. Compon., Packag. Manuf. Technol.*, vol. 2, no. 4, pp. 539–547, Apr. 2012.

[25] Y. Lin et al., "Temperature- and degradation-dependent maximum electric field stress in wire-bonding power modules under PWM waves," *IEEE J. Emerg. Sel. Topics Power Electron.*, vol. 10, no. 6, pp. 7653–7664, Dec. 2022.

[26] Y. Ding, Y. Wang, H. Sun, and Y. Yin, "High-temperature partial discharge characteristics of power module packaging insulation under square pulse with high DV/DT based on down-mixing method," *IEEE Trans. Ind. Electron.*, vol. 70, no. 7, pp. 7334–7342, Jul. 2023.

[27] D. M. Min et al., "Interfacial regions and network dynamics in epoxy/POSS nanocomposites unravelling through their effects on the motion of molecular chains," *Composites Sci. Technol.*, vol. 199, 2020, Art. no. 108329.

[28] Y. Wang et al., "Space-charge accumulation and its impact on high-voltage power module partial discharge under DC and PWM waves: Testing and modeling," *IEEE Trans. Power Electron.*, vol. 36, no. 10, pp. 11097–11108, Oct. 2021.

[29] Z. Shen et al., "Phase-field modeling and machine learning of electric-thermal-mechanical breakdown of polymer-based dielectrics," *Nature Commun.*, vol. 10, no. 1, 2019, Art. no. 1843.
[30] Z. Shen et al., "High-throughput phase-field design of high-energy-density polymer nanocomposites," *Adv. Mater.*, vol. 30, no. 2, 2018, Art. no. 1704380.

Qilong Wang (Graduate Student Member, IEEE) was born in Sichuan, China, in 1998. He received the B.S. degree in North China Electric Power University, Beijing, China, in 2020. He is currently working toward the Ph.D. degree at the College of Electrical Engineering, Zhejiang University, Hangzhou, China.

His main interest includes power electronics packaging insulation.

Xiangrong Chen (Senior Member, IEEE) was born in Hunan, China, in 1982. He received the M.S. and Ph.D. degrees in electrical engineering from Xi'an Jiaotong University, Xi'an, China, in 2008 and 2011, respectively.

He was a Postdoctoral Researcher in 2011, an Assistant Professor from 2012 to 2016, and an Associate Professor in 2016 in high-voltage engineering with the Department of Manufacturing and Materials Technology, Chalmers University of Technology, Gothenburg, Sweden. Since 2017, he has been a One Hundred Talents Researcher/Professor with the College of Electrical Engineering, Zhejiang University (ZJU), Hangzhou, China. He was the Vice-Dean of the ZJU-UIUC Institute from 2020 to 2021 and has been the Head of the Institute of Power System Automation, ZJU, since March 2020. His research interests include advanced electrical materials and high-voltage insulation testing technology, advanced power equipment and new power system, and advanced high-voltage technology.

Dr. Chen has been an Associate Editor of IEEE TRANSACTIONS ON DIELECTRICS AND ELECTRICAL INSULATION since May 2021.

Ashish Paramane (Senior Member, IEEE) was born in India in 1991. He received the M.Tech. degree in power systems engineering from Dr. Babasaheb Ambedkar Technological University, Lonere, India, in 2014, and the Ph.D. degree in high voltage engineering from VIT University, Vellore, India, in 2018.

He was a Postdoctoral Research Fellow with the Advanced High Voltage Technology Laboratory, College of Electrical Engineering, Zhejiang University, Hangzhou, China, from 2019 to 2021. He is currently working as an Assistant Professor with the Electrical Engineering Department, National Institute of Technology, Silchar, India.

His research interests include partial discharge, electrical tree, and space charge properties of nanodielectrics.

Junye Li received the B.S. and Ph.D. degrees in engineering thermophysics from Zhejiang University, Hangzhou, China, in 2014 and 2020, respectively.

He is currently a Technology Specialist with ZJU-Hangzhou Global Scientific and Technological Innovation Center.

His research interests include numerical and experimental study of electronic cooling.

Xiaofan Huang was born in Sichuan, China, in 1999. She received the B.S. degree from Southwest Jiaotong University, Chengdu, China, in 2021. She is currently working toward the Master's degree with the College of Electrical Engineering, Zhejiang University, Hangzhou, China.

Her main interests include power electronics packaging materials and high-voltage cable insulation materials.

Na Ren (Senior Member, IEEE) received the B. Sc. degree from Wuhan University, Wuhan, China, in 2010, and the Ph.D. degree from Zhejiang University, Hangzhou, China, in 2015.

She was a Postdoctoral Researcher with University of California, Los Angeles, CA, USA, between 2016 and 2019. She is currently an Associate Professor with Zhejiang University. Her current research interests include SiC power semiconductor device designs, manufacturing process, and reliability enhancement.